JOURNAL OF APPLIED PHYSICS **117**, 054504 (2015)

Cu impurity in insulators and in metal-insulator-metal structures: Implications for resistance-switching random access memories

Sumeet C. Pandey,[a] Roy Meade, and Gurtej S. Sandhu
Emerging Memory Group, Process R&D, Micron Technology Inc., Boise, Idaho 83707-0006, USA

(Received 6 October 2014; accepted 26 January 2015; published online 4 February 2015)

We present numerical results from atomistic simulations of Cu in SiO_2 and Al_2O_3, with an emphasis on the thermodynamic, kinetic, and electronic properties. The calculated properties of Cu impurity at various concentrations ($9.91 \times 10^{20}\,cm^{-3}$ and $3.41 \times 10^{22}\,cm^{-3}$) in bulk oxides are presented. The metal-insulator interfaces result in up to a ~4 eV reduction in the formation energies relative to the crystalline bulk. Additionally, the importance of Cu-Cu interaction in lowering the chemical potential is introduced. These concepts are then discussed in the context of formation and stability of localized conductive paths in resistance-switching Random Access Memories (RRAM-M). The electronic density of states and non-equilibrium transmission through these localized paths are studied, confirming conduction by showing three orders of magnitude increase in the electron transmission. The dynamic behavior of the conductive paths is investigated with atomistic drift-diffusion calculations. Finally, the paper concludes with a molecular dynamics simulation of a RRAM-M cell that attempts to combine the aforementioned phenomena in one self-consistent model. © *2015 AIP Publishing LLC*. [http://dx.doi.org/10.1063/1.4907578]

I. INTRODUCTION

Resistance switching memories have emerged as potential non-volatile memory technology with data retention and endurance performance that exceeds that of NAND flash. High-speed switching and low set/reset current are some of the promising characteristics of such devices.[1] There are two categories of Resistance-Switching Random Access Memories (RRAM): oxygen vacancies in transition metal-oxides (RRAM-Ox), and electrochemically active metal-ion impurities in electrolyte/dielectrics (RRAM-M). RRAM-M is typically based on migration and clustering of ionized Cu through an insulator under applied electric fields in order to induce switching of the resistance states of the memory cell. It has been postulated that in the ON state, the Cu ions injected into the dielectric under an electric field form a localized conductive path (i.e., filamentary pathway), and the OFF state is achieved by dissolution of the conductive path upon field reversal.[1,2]

The RRAM-M cell structure is challenging to study via traditional analytical techniques, leading researchers to use alternative approaches to understand the fundamental mechanisms involved. The structure itself is typically simple, comprising of a metal-insulator-metal (MIM) stack. Even the dielectric material is straightforward, with Al_2O_3 being a promising candidate among others.[29] However, for RRAM-M cells of industrial interest, the dielectric thicknesses tend to be thin, less than 3 nm.[1,29] Thicker films lead to higher forming voltages, an added challenge for on-pitch CMOS. Additionally, a thicker dielectric film contributes to a thicker overall MIM cell. NAND devices are currently shipping with half-pitch critical dimensions less than 20 nm. Therefore, the industry is searching for a cross-point RRAM-M cell that can scale well below the 20 nm process node. Thus, the overall MIM stack height must be less than 20 nm in order to maintain a manageable aspect ratio for process nodes with a half-pitch much less than 20 nm. Finally, the localized filament is presumed to form in the insulating layer, making the filament small and difficult to image. Imaging of a conductive filament without altering its characteristics is challenging, even at the stage of locating it in the device. For these reasons, researchers have turned to multi-scale modeling to study RRAM-M phenomena. The authors hope to present various calculations and techniques that could provide insight into the microscopic mechanisms that govern the operation of RRAM-M cells.

In order to understand RRAM-M device operation, the formation energetics, electronic structure, and response to electric field must be studied for metallic impurities in insulators. The role of oxygen vacancies in influencing the electronic structure towards filamentary conduction in transition metal oxides based RRAM has been theoretically examined previously for TiO_2 and NiO. The ON conduction was concluded to be driven by the ordering of oxygen vacancies and the conduction was described by defect-assisted electron tunneling.[3] Electrochemically active Cu in SiO_2 and Al_2O_3 has been experimentally investigated for memory applications, and various empirical and some first-principles models have been proposed to explain the operation.[4–7] However, an atomically detailed electronic structure and transport linking to resistance states, retention, migration under fields, and effect of metal/insulator interfaces on electron and ion transport have not been studied and reported in the literature. In ultra scaled devices below 10 nm, the interfaces are critical in determining the defect formation thermodynamics, electrostatics, and transport properties. To this end, we have performed density-functional theory (DFT) calculations to

[a]Author to whom correspondence should be addressed. Electronic mail: spandey@micron.com

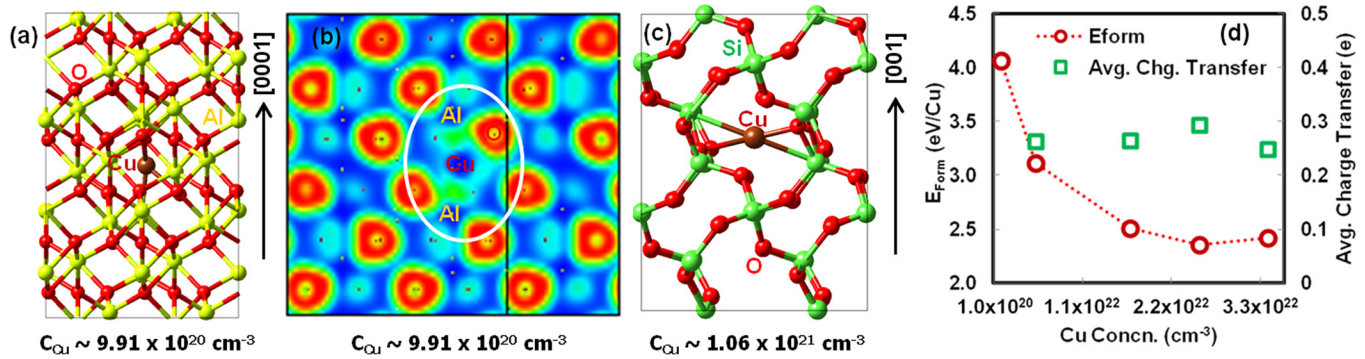

FIG. 1. (a) Structure of a single Cu impurity in a c-Al_2O_3 (R-3c) $2 \times 2 \times 1$ super-cell. Red, brown, and yellow spheres represent O, Cu, and Al atoms, respectively. (b) Electron localization function in the plane passing through the center of the Cu impurity bonded to Al and O. Blue-green-red represents low-medium-high electron concentration from 0-0.5 to 1.0 e/Å^3, respectively. (c) Cu interaction with Si and O in α-quartz c-SiO_2. Red, brown, and green spheres are O, Cu, and Si atoms, respectively. (d) The computed formation energy (eV per Cu atom) (circles) and the average charge transfer (squares) as a function of Cu impurity concentration in SiO_2.

systematically study the effect of Cu impurity inclusions in the dielectric on the electronic structure and the electron transport in MIM structures. Moreover, the initial forming kinetics is studied through molecular dynamics simulations based on charge-optimized many-body (COMB) potential.

II. RESULTS AND DISCUSSION

A. Materials and structures

Using DFT, a systematic set of calculations was performed to study Cu in Al_2O_3, and SiO_2 in bulk oxides and in MIM structures. The DFT calculations were carried out using the code Vienna *ab initio* simulation package (VASP)[11] and the structural results reported were obtained within the generalized gradient approximation (GGA) with the Perdew-Burke-Ernzerhof (PBE)[12] exchange and correlation functional. Plane-wave basis sets were employed for expanding the electronic wavefunctions and the projector augmented-wave method (PAW)[13] was used for treating the ionic cores.

The DFT optimized $2 \times 2 \times 1$ cell of crystalline Al_2O_3 (R-3c space group) with a single Cu impurity is shown in Fig. 1(a). The lattice constants for the unit cell are calculated to be $a = b = 4.81$ Å, $c = 13.12$ Å, $\alpha = \beta = 90°$, and $\gamma = 120°$. In c-Al_2O_3, there are two types of voids that can act as possible sites for interstitials, corresponding to a radii of 0.74 Å and 0.46 Å, respectively. Out of these two possible occupancies, the voids with a radii of 0.74 Å were calculated to be energetically more favorable for Cu interstitials in a dilute limit, and hence, were used as an initial guess for the initial state (IS) of the Cu ion in alumina. Starting from this, the coordinates of Cu ion were further relaxed to the minimum energy location using the conjugate gradient method. The Cu appear to occupy a slightly off-centered site with respect to the Al atoms that are aligned along [0001], wherein, the $d_{Cu\text{-}O} \sim 1.99$ Å and $d_{Cu\text{-}Al} \sim 2.21$ Å. The electron localization function projected on the plane passing through the center of this Cu impurity shows (Fig. 1(b)) that Cu-O interaction is predominantly ionic mixed with covalent character, whereas the Cu-Al interaction is metallic. In the case of a $2 \times 2 \times 1$ quartz-SiO_2 (unit cell: $a = b = 4.605$ Å, $c = 10.41$ Å, $\alpha = \beta = 90°$, and $\gamma = 120°$), the Cu interstitials relax such that the $d_{Cu\text{-}O}$ is ~2.07 Å and $d_{Cu\text{-}Si}$ is ~2.55 Å, as depicted in Fig. 1(c). The electronic formation energy, ΔE_f, of Cu interstitial impurity in c-Al_2O_3 was calculated to be 8.58 eV, which is higher than the value in c-SiO_2 of 6.03 eV. The

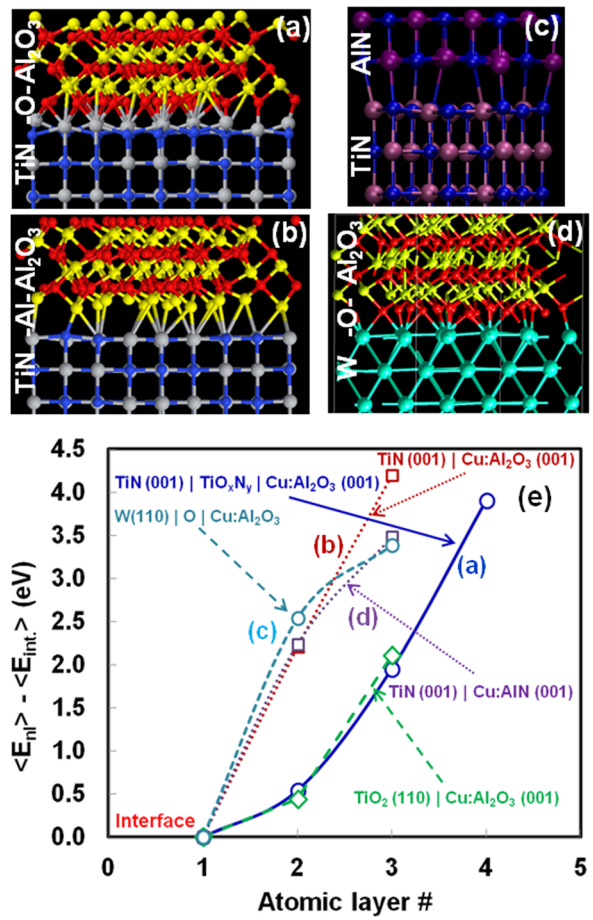

FIG. 2. Atomic structure of various metal-insulator interfaces: (a) TiN (001)|Al_2O_3 (001) O-terminated, (b) TiN (001)|Al_2O_3 (001) Al-terminated, (O: red, Al: yellow, Ti: grey, and N: blue), (c) TiN (001)|AlN (001), (Al: maroon, Ti: purple, and N: blue), (d) W (110)|Al_2O_3 (001) O-terminated (W: cyan), (e) relative changes of energies for Cu occupation (9.91×10^{20} cm^{-3}) in different atomic layers near the metal/insulator interfaces.

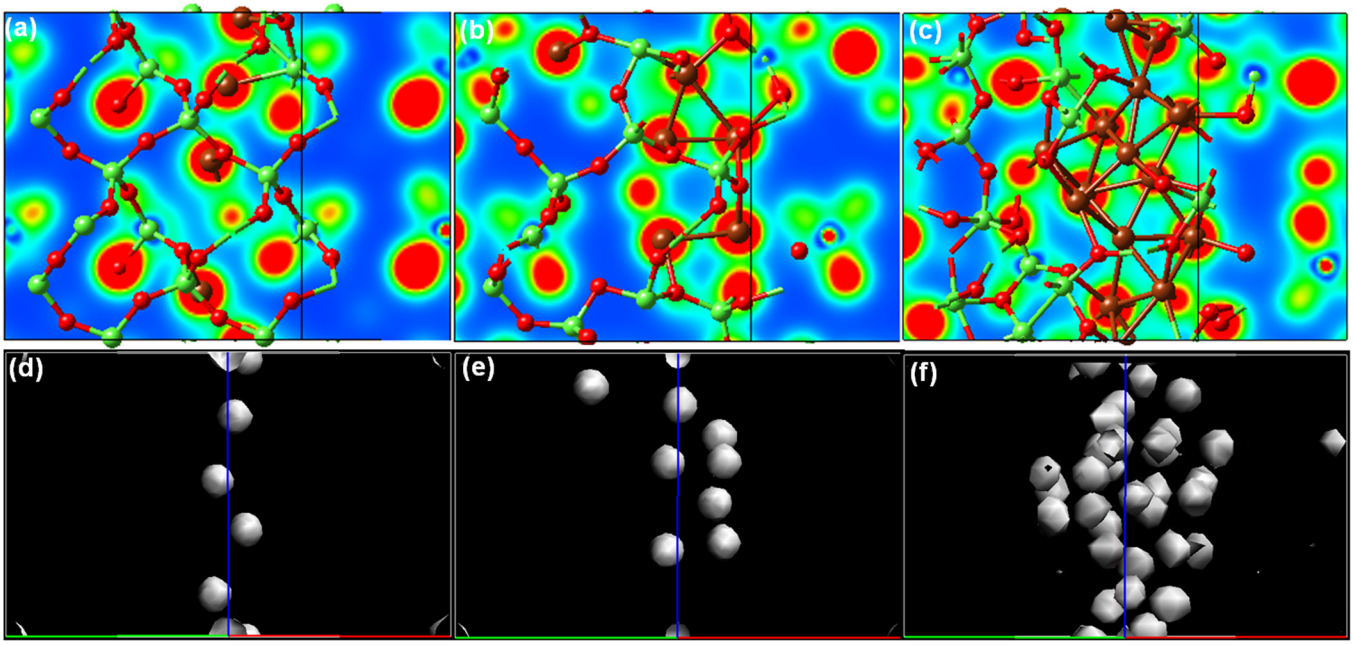

FIG. 3. Total valence charge density in the (100) plane (top (a)–(c): blue-green-red represents low-med-high charge densities, respectively) and the corresponding partial charge density isosurfaces around $E_F \pm 0.1$ eV (bottom (d)–(f)) for clustered Cu impurities in SiO_2 corresponding to the impurity concentration of: (a) $5.32 \times 10^{21}\,cm^{-3}$, (b) $8.52 \times 10^{21}\,cm^{-3}$, and (c) $3.41 \times 10^{22}\,cm^{-3}$.

chemical potential of Cu in the bulk metal electrode was used as reference for ΔE_f comparisons. Furthermore, a less dense $2 \times 2 \times 1$ quartz-SiO_2 (unit cell: $a = b = 4.97$ Å, $c = 10.97$ Å, $\alpha = \beta = 90°$, and $\gamma = 120°$) yielded an even lower ΔE_f of 4.06 eV. The results point to a lower and higher forming voltage requirement for the lower-density c-SiO_2 and c-Al_2O_3, respectively, relative to the quartz-SiO_2 ($a = b = 4.605$ Å, $c = 10.41$ Å, $\alpha = \beta = 90°$, and $\gamma = 120°$). As a function of Cu impurity concentration in c-SiO_2 (Fig. 1(d)), this formation energy, E_f (eV/Cu), shows an overall decrease up to 2.35 eV at $2.55 \times 10^{22}\,cm^{-3}$. We observe a tendency for an increased Cu interaction to lower the E_f, which suggests a reduced thermodynamic barrier to injection of Cu impurities as the Cu concentration increases. This also accompanied an increased stability of their structural arrangements. The average charge transfer of Cu to SiO_2 in such structures was calculated to be ~0.25–0.29e.

As the devices are scaled down to below 10 nm with individual material layers becoming a few Å thick, the role of interfaces is becoming increasingly critical as they tend to determine the physical properties of the entire system. In addition to electrostatics and electron transport, the interfaces are crucial in shaping the resistance states and ion transport in MIM structures. In Fig. 2, we show the various metal-insulator interfaces studied and the relative energies for Cu occupation ($9.91 \times 10^{20}\,cm^{-3}$) in the various atomic layers (originating from the interface to the relative bulk of the insulator). Within the systems studied, Cu energetically favored the interface in all the structures due to the mechanical strain relaxation and the lower exchange energy (as a consequence of the availability of delocalized electrons in the metallic electrodes). There exists a thermodynamic driving force towards the interface for Cu occupation, which is lower for the oxygen-rich interfaces compared to the metal-rich counterpart. Exception to this observation is the case of W metal electrode, which is known to be quite difficult to oxidize. Overall, the results suggest a higher probability for Cu accumulation at the interfaces (during operation). Additionally, the presence of oxygen near the metal electrodes tends to lower the Cu potential in the near atomic layers. As a consequence, during the reversal of field (reset operation), the dissociation of the Cu cluster is expected to occur in the relative bulk of the insulator (about ~3 atomic layers further away from the interfaces) where the potential is qualitatively calculated to be the highest.

B. Electronic density of states (DOS): Effect of concentration and order

For calculation of the electronic density of states, hybrid functional as in Heyd-Scuseria-Ernzerhof[14] (HSE06) was employed. These functional mixes Hartree-Fock (HF) exchange with the GGA exchange and correlation in the short-range portion of the potential to yield better estimates of the band gaps in semiconductors. Both crystalline and amorphous forms were investigated as required. In Fig. 3, we show the total valence charge density [ρ^{TVCD}] (a)–(c) and the corresponding partial charge density [ρ^{PCHG}] isosurfaces (0.05–$0.08\,e/Å^3$) around the eigen values of $E_F \pm 0.1$ eV (d)–(f) for Cu impurity aggregated in SiO_2(110). The Cu concentration is examined in the range of $5.32 \times 10^{21}\,cm^{-3}$–$3.41 \times 10^{22}\,cm^{-3}$. The charge densities around $E_F \pm 0.1$ eV is observed to be bound on Cu for lower concentrations; the copper's interaction (bonding) with the surrounding matrix leads to localized electron states. With the increase in the number of neighboring Cu, these localized states increasingly interact with each other as expected. The local concentration of metallic impurity determines the

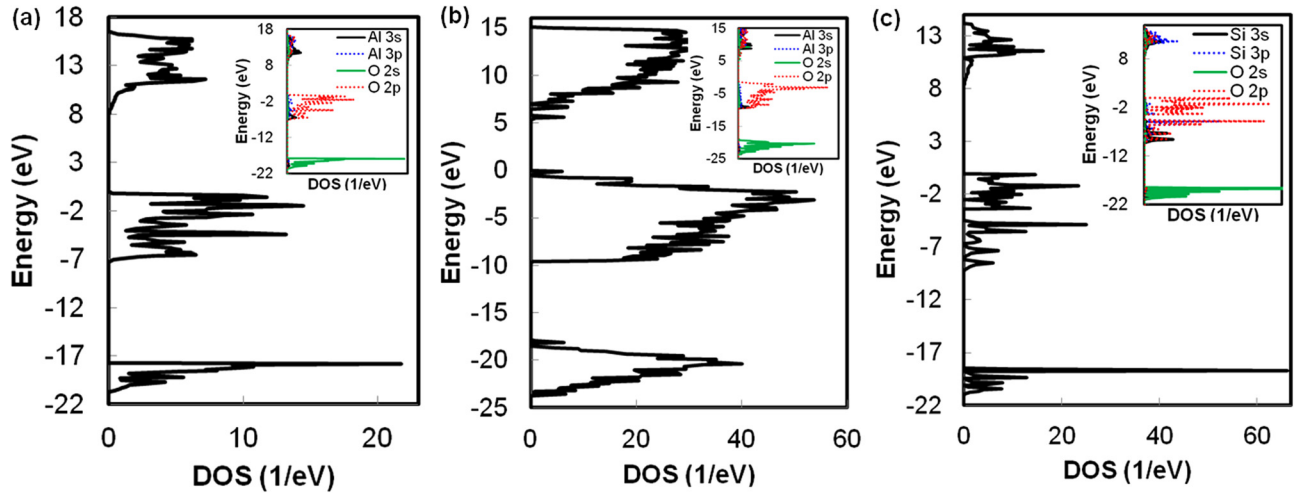

FIG. 4. Total (solid-black lines) and partial (inset) density of states computed with HSE06 for: (a) c-Al_2O_3 (R-3c), (b) a-Al_2O_3; in the inset, the solid-blue, solid-green, and dashed-red lines represent Al 3s, O 2s, and O 2p, respectively. (c) α-quartz SiO_2; in the inset the solid-black, dashed-blue, solid-green, and dashed-red lines represent Si 3s, Si 3p, O 2s, and O 2p, respectively.

localization/delocalization of electronic states. Interestingly, the Cu clusters within the insulator arrange in configurations similar to the lowest-energy FCC-Cu (111) units. The increase in the delocalization of the ρ^{TVCD} can be seen (green intermediate regions) with increasing Cu coordination as the cluster size increases indicating an accompanied higher metallic character. Importantly, both Cu concentration and coordination with other Cu impurities within the insulator are shown to determine the chemical bonding and the available overlapping states for charge carrier conduction around the Fermi level. Similar charge-density characteristics were noted for Cu ordering in (1231) for c-Al_2O_3.

The total and partial DOS computed with HSE06 for c-Al_2O_3 (R-3c), a-Al_2O_3, and c-SiO_2 (quartz) are depicted in Fig. 4. Three distinct bands appear in the TDOS for both c-Al_2O_3 (R-3c) (Fig. 4(a)) and a-Al_2O_3 (Fig. 4(b)). The lower valence band (LVB), upper valence band (UVB), and the conduction band (CB) primarily consist of O 2s, O 2p, and Al 3s states, respectively, as shown in the PDOS in the inset. The ionic bonding is predominant in the oxide with some covalent character from Al 3s and O 2p hybridization in the CB and UVB. Moreover, the a-Al_2O_3 (Fig. 4(b)) in comparison with c-Al_2O_3 (R-3c) shows an increased band-width. The disorder induced tails and states in the gap near the band edges reduce the computed band gap from ∼8.14 eV (for crystalline) to ∼6.3 eV (for amorphous counterpart). The calculated E_g for c-Al_2O_3 is comparable to 8.8 eV obtained from experimental measurement;[23] however, wide-ranging values of E_g for a-Al_2O_3 are reported in the literature. Notably, a recent study[24] based on internal photoemission and spectroscopic ellipsometry reports a E_g in the range of ∼6.11–6.31 eV, which is in quite good agreement with our results. It is also worth mentioning that experimentally determined E_g typically show an additional dependence on the choice of deposition method, film density, and film thicknesses. Nevertheless, the lower E_g for the amorphous systems is consistent with the explanation of a lack of long-range order and distribution of coordination (bond lengths and angles) in amorphous systems.[25] For the quartz c-SiO_2, the UVB splits into sub bands exhibiting a higher covalent character than the c-Al_2O_3. The Si 3s–O2p hybridization is observed in the lower UVB, and Si 3s, Si 3p, and O 2p states form the CB. The computed $E_g \sim 7.9$ eV is underestimated in comparison with the experimental[26] value of ∼9.6 eV. Notably, these E_g calculations based on HSE06 can be improved to give an exact agreement with experiments using optimized mixing parameters of ∼0.31 for c-Al_2O_3 and ∼0.38 for c-SiO_2.[27] We have selected a value of 0.25 throughout in this work to allow for consistent comparisons.

The injected Cu interstitials in SiO_2 create Cu 3d-O 2p hybridized states near the top of the VB, and Cu 4s states (along with Si 3s, 3p, and O 2p) at the bottom of the CB. This is in addition to the induction of localized states in the gap near the valence band maximum (VBM) and the conduction band minimum (CBM) as shown in Fig. 5(a), corresponding to $C_{Cu} \sim 8.52 \times 10^{21}\,cm^{-3}$. The Cu only PDOS is shown in the inset, which shows dominant contribution to the DOS in the top of the valence band (TVB), CB, and the in-gap states. With an increase in C_{Cu} to $\sim 1.7 \times 10^{22}\,cm^{-3}$, Fig. 5(b), the number of localized states within the gap increases, and a complete closure of the gap having fully metallic character is attained at the concentration of $C_{Cu} \sim 3.41 \times 10^{22}\,cm^{-3}$, as shown in Fig. 5(c).

C. Ionic drift under electric fields

In addition to formation energies, the ionic transport under electric fields will affect the conductive path morphology and conductivity; therefore, an examination of ionic drift was also performed. Typically, the drift velocity of an ion under an electric field, E, is approximated in the literature to have a linear and exponential dependence on E under the low-field and high-field regimes, respectively.[8] Moreover, Strukov and Williams specifically studied the exponential dependence of switching speeds in a memristor using a phenomenological nonlinear-ionic-drift model.[9] Their rigid point-ion exponential model was used to explain very large ratios for the state-lifetime to the speed-of-resistance-switching. More

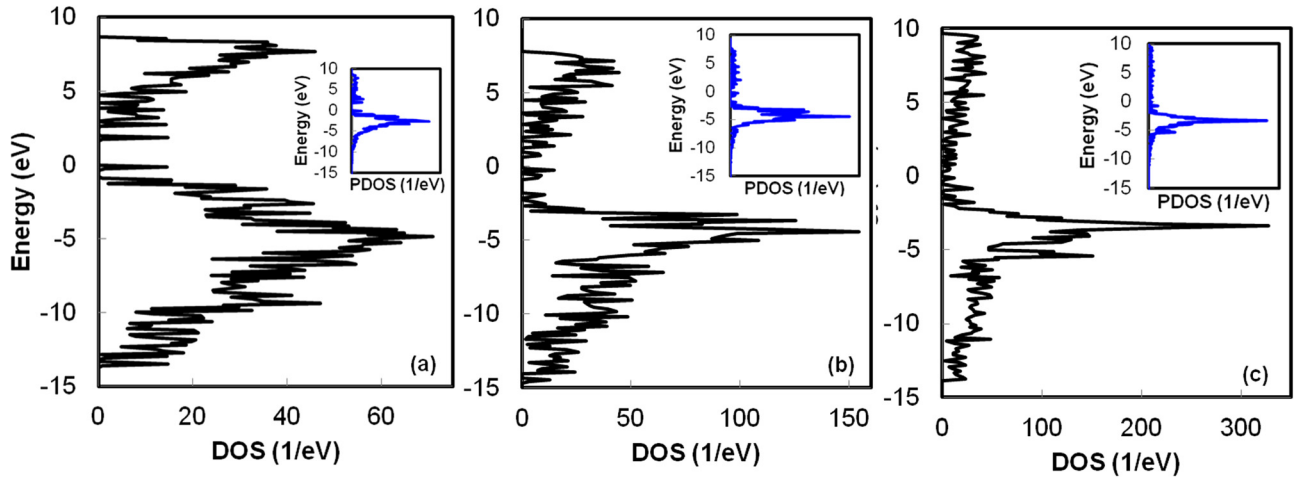

FIG. 5. Total (solid-black lines) and Cu partial (inset) density of states in Cu:SiO_2 computed with HSE06 for Cu concentrations: (a) $8.52 \times 10^{21}\,cm^{-3}$, (b) $1.7 \times 10^{22}\,cm^{-3}$, and (c) $3.41 \times 10^{22}\,cm^{-3}$.

importantly, the authors stated the shortcomings of the Mott-Gurney[10] model, which best describes purely ionic crystal. In addition, the authors discussed the possibility of using the nudged-elastic band method for covalent and mixed covalent/ionic crystal. To this end, we have performed DFT calculations of Cu ion migration in Al_2O_3 under the application of an external electric field. We have determined the quantitative lowering of the barrier and have subsequently fitted a simple mathematical expression to capture this effect. The simple equation does not fully describe the non-linear field-induced barrier-lowering; however, it allows for an expression appropriate for the purposes of phenomenological process and device modeling.

For estimating the activation energies for diffusion, the statistical method, namely, the Transition State Theory (TST) proposed by Eyring[18] was selected. Diffusion processes are rare events with transitions occurring orders of magnitude slower than the atomic vibrations, hence, the direct dynamical simulations are not practical within DFT. Consequently, an alternative is needed, with TST being the most commonly adopted statistical approach for such studies. TST relies on the assumption of the existence of a dividing surface (transition state) between reactants and products. This dividing surface can be chosen to be orthogonal to the normal mode with imaginary frequency at the saddle point, making the saddle point a local maximum of the potential energy surface (PES) on the dividing surface (transition state). Using the harmonic approximation, an Arrhenius type equation for the transition rates can be obtained. Thus, one needs to accurately search for saddle points of the corresponding PES to characterize a diffusion event. This saddle point between two minima of the PES can be numerically identified by locating the highest point on the minimum energy path (MEP). To establish the saddle point rigorously, Henkelman and coworkers[19] introduced the climbing-image nudged elastic band method (CI-NEB) as an improvement to the nudged elastic band (NEB) method. In our choice of method, the CI-NEB, after some iteration similar to the NEB, the highest energy is chosen for the purposes of climbing up to the saddle.

In order to include the effect of electric fields on ion transport, we have to consider some additional complexity. Upon introduction of electric field into the DFT Hamiltonian, the potential energy loses its periodicity and the Bloch's theorem loses its validity in a strict sense. This is in addition to the ground state being ill-defined as potential energy is not bounded from below.[15] The situation is treated by using perturbation theory, where, electric field acts as a singular perturbation on the electronic wave functions.[16,17] The solution seeks long-lived resonances by solving for the field-polarized Bloch functions through minimization of the electric enthalpy functional. The minimization is performed using perturbation theory for the static response of the insulating crystals to a finite homogeneous electric field. The method used in our analysis for the treatment of electric field is implemented in VASP as a variant of the perturbation expansion after discretization approach (PEAD).[16] It is worth mentioning that there are numerical limitations to this approach with respect to the *k*-point sampling and electric field strengths that can be treated. However, this study has been carried out well within such method limitations by restricting the study to reasonable e-field values. The induced macroscopic polarization is calculated as the Berry phase polarization in the quantum mechanical framework proposed by King-Smith and Vanderbilt.[15]

The calculations we discuss quantify the field-induced barrier-lowering and draw comparisons with the hypothesis of Mott-Gurney.[10] The Cu (brown atom) in its optimized IS and Final State (FS) is slightly off-centered with respect to the O atoms and is bonded to 3 O atoms and an Al atom, as shown in Figs. 6(a) and 6(c), respectively. An adjacent site has been selected as the FS, such that a single transition state exists between the IS and the FS that is separated by a jump distance, d. Fig. 6(b) shows the interstitial Cu ion at the transition state that corresponds to the saddle point that determines the activation energies (barriers), Ea, of Fig. 6(d). Fig. 6(d) shows the energy profile (as a function of migration coordinate) for a representative Cu ion migration pathway in a c-Al_2O_3 super-cell. As the strength of

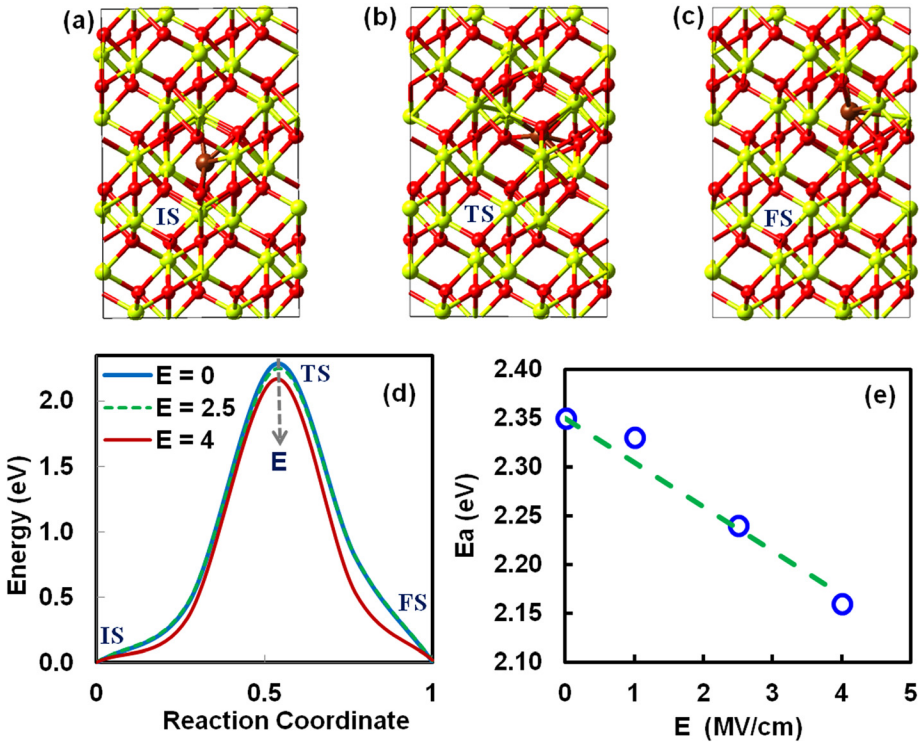

FIG. 6. (a) Initial, (b) transition, and (c) final states for Cu ion during a hop to the nearest void. (d) Energy profile as a function of reaction coordinate along a pathway of a Cu ion migrating in c-Al_2O_3. Yellow, red, and brown spheres are used to denote Al, O, and Cu, respectively. (e) Activation energies for Cu migration in the bulk of Al_2O_3 as a function of the E-field (in the range of 0-4 MV/cm). The E-field is applied along the direction of the motion of Cu ion. The solid circles represent the calculated values of the effective barriers with dashed and solid line depicting the linear and quadratic fit to the computed values.

the applied electric field is progressively increased from no field to 4 MV/cm (blue solid-line to red solid-line in Fig. 6(d)), the energy profiles exhibit a field-induced lowering of the barrier. The motion of interstitial Cu ions along a uniform field has been quantified in the plot of E_a (eV) as a function of field strengths that are parallel to the direction of Cu hopping, E (MV/cm), as shown in Fig. 6(e). The DFT (TST+PEAD) calculated values are compared to a linear fit (in a similar spirit to that of Mott and Gurney[10]) and a quadratic fit. In the absence of field, the calculated E_a is 2.35 eV in c-Al_2O_3. Under a field, the E_a gets significantly reduced by as much as ~0.2 eV under the variation of E-field from 0–4 MV/cm.

For ionic (polar) crystals, Mott and Gurney had proposed that the barrier height for drift of a lattice defect under an external field in the direction of the field and against the field can be modified by ±(1/2)*qFd, respectively. According to their work, in the case of motion along the field, the barrier lowering can be expressed as, $E_a = E_a^0 - \frac{1}{2}$qFd, where q is the charge on the ion, F is the applied external field, and d is the distance between adjacent lattice positions for defects. However, our calculations for Al_2O_3 (a dielectric with a mixture of ionic and covalent characteristics) suggest that the first order approximation of a field dependence of the effective E_a may be estimated from a Mott-Gurney-like model that includes in addition a properly selected component of the dielectric constant tensor, ε. The ε relates the macroscopic electric field to the microscopic local electric field, given as, $E_a = E_a^0 - q\varepsilon$Fd. This material-dependent static dielectric constant for c-Al_2O_3 is computed within PBE to be $\varepsilon \approx 3.1$, which is in good agreement with the value of $\varepsilon \approx 3.4$ obtained from the linear fitting using q ≈ 0.35e as derived from the Bader charge analysis.

D. State stability and data retention

Under the electrochemical driving forces (electric and chemical potential), various configurations for the electrochemically active metal impurities can be achieved within the MIM structures based on the external stimulus and the corresponding ionic and electronic relaxation. The clustered morphology attained as a consequence of kinetics under thermal and electric fields determines the stability of these states and the corresponding conductance. Figs. 7(a) and 7(b) show a mechanism wherein the lower-resistance state (LRS) destabilizes (retention loss) due to the dissociation and diffusion of the least-coordinated Cu ion from the narrowest part of a clustered configuration –$[Cu]_n$–, such that, the dissociated Cu is ~>0.4 nm distant from the metallic cluster (thereby attaining a relative higher resistance state (HRS)). The presence of asymmetric twin-wells (Fig. 7(c)) arising out of Cu-Cu bonding renders the LRS as the more stable state yielding an activation energy barrier of 1.6–1.8 eV for the LRS retention loss. The activation energy barrier of 1.6–1.8 eV implies retention of the data state that exceeds the typical requirement of 10 yr at 85 °C for its application in a non-volatile memory. The switching from LRS to HRS is driven by overcoming of this barrier through the assistance of local electric field and temperature. When Cu ion dissociates from the cluster (filament/conductive-bridge), this accompanies a change in the oxidation state of the Cu ions involved and local reorganization of Cu and the dielectric. In addition to the diffusion activation energy barriers, there is an additional dissociation energy penalty due to a lower chemical potential in the clustered state that makes the twin-wells asymmetric and hence favors the LRS. Fig. 7(d) points to a similar tendency in c-SiO_2, where the Cu shows an attractive pair correlation of 1.13 eV in a spin-polarized calculation of interacting and distant configurations. Consistent with this

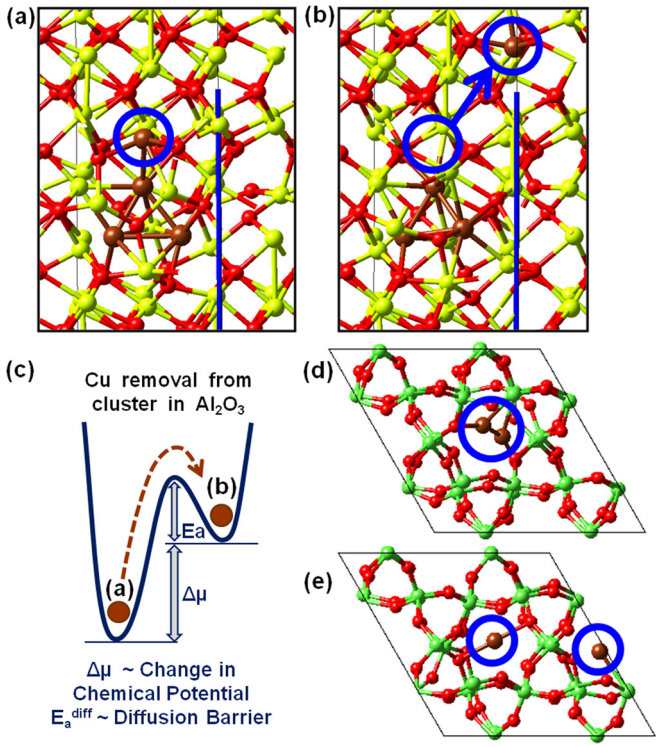

FIG. 7. Atomic structure of Cu clusters in (a) c-Al_2O_3 in an aggregated (LRS) state, (b) in a dissociated (HRS) state, (c) schematic of the underlying energetics transitioning from (a) to (b). Cu pair in an (d) aggregated state and (e) dissociated state in c-SiO_2. Red, brown, yellow, and green spheres represent O, Cu, Al, and Si, respectively.

result, a higher stability of the LRS, and alternatively the failure of HRS towards LRS have been observed in retention experiments at 85 °C for the Cu-SiO_2-Pt RAM.[28] However, it should be noted that this potential landscape may be modified by the local Cu concentration and coordination, as well as, the temperature that can change the relative stability of the states. To examine the additional effect of structure on the diffusion barriers, we compare the amorphous and crystalline Al_2O_3. The calculated E_a (using the mean squared displacement (MSD) technique) for diffusion of Cu is 0.34–0.5 eV in a-Al_2O_3, which is much lower compared to that of the 2.35 eV in c-Al_2O_3 (R-3c) (calculated with TST). This indicates the strong influence of structure and density on these barriers, hence, the importance of material properties in determining device characteristics.

E. Conduction mechanism and non-equilibrium electron transport

The electron transport within the phase-coherent approximation of non-equilibrium Green's function (NEGF) is computed with Atomistix ToolKit (ATK)[20] that employs numerical localized atomic basis sets. For this study, single zeta polarized (SZP) sets were employed with Perdew-Zunger parameterized local density approximation (LDA) for the exchange-correlation. The MIM device structure was relaxed for the central region such that the force on each atom was less than 0.02 eV/Å. $4 \times 4 \times 100\,k$-points mesh was used for the calculation of device density of states and transmission spectra.

To quantify the effect of injected Cu impurity aggregates on electron transport in MIM structures, we compare the pristine and formed states in a Cu-SiO_2-Pt structure with an insulator thickness of ~1.3 nm, as shown in Fig. 8. The pristine MIM has no Cu within the insulator (Fig. 8(a)) and consists of 12 atomic layers of Cu in the scattering region. For the formed case, the MIM structure is geometrically optimized assuming the Cu to be clustered and ordered due to the effect of chemical potential and the local electric fields (Fig. 8(b)). The corresponding local density of states (LDOS) at the Fermi level shows no states for transport in the pristine case (Fig. 8(c)), whereas a contiguous LDOS is clearly observed within the insulator in the formed MIM (Fig. 8(d)). The formed LDOS is primarily located on the Cu cluster; however, the Si and O states nearby also get perturbed due to the interactions with Cu. Also, the projected device density of states (PDDOS) exhibit an obvious peak near the Fermi level (E = 0) for the formed case that is absent in the pristine MIM. Importantly, the two states yield transmissions that are more than 3 orders of magnitude different, such that, T_F/T_P $(E = E_f) \sim 1.95 \times 10^3$. Expectedly, we observe a large conductance variation due to the inclusion of Cu aggregates in the insulator.

F. Molecular dynamics simulations

One of the important requirements for developing a rigorous methodology to study RRAM-M devices involves capability to simulate dynamical processes over nanoseconds (ns) in a heterogeneous MIM system consisting of a few thousand atoms. This limits a full *ab initio* treatment of the problem and calls for use of methodology that are based on force-field (FF) and tight binding (TB) schemes. Many-body interatomic potential fitted to reproduce fundamental DFT energetics and electronic charges is a computationally less-expensive technique, which in turn can be used for molecular dynamics simulations under applied electric fields. The description of the force-field employed in this work allows for reactive bond breaking and forming processes; variable charge equilibration; capturing of bonding in metallic, ionic, and covalent states; ionization under non-equilibrium conditions; as well as charge transfer across heterogeneous interfaces. As implemented in the Large-scale Atomic/Molecular Massively Parallel Simulator (LAMMPS),[21] we have used the reparameterized COMB[22] potentials to model the Cu|SiO_2|X (X = inactive metal electrode) cells. The COMB formalism describes the total potential energy of the system by the summation of: self-energy of atoms, interatomic potential between the atoms, and the bond-bending terms. The interatomic potential includes the short-range repulsion, short-range attraction, and the long-range Coulombic interaction. In this scheme, the many-body effects are captured by the bond-order term in the short-range attraction term, and the long-range Coulombic interaction between ions is accounted for with the charge coupling factor. Energy that is required to form a charge is taken into account as a self-energy term with coefficients that are fitted to the atomic ionization energies and electron affinities. Bond-bending penalties are

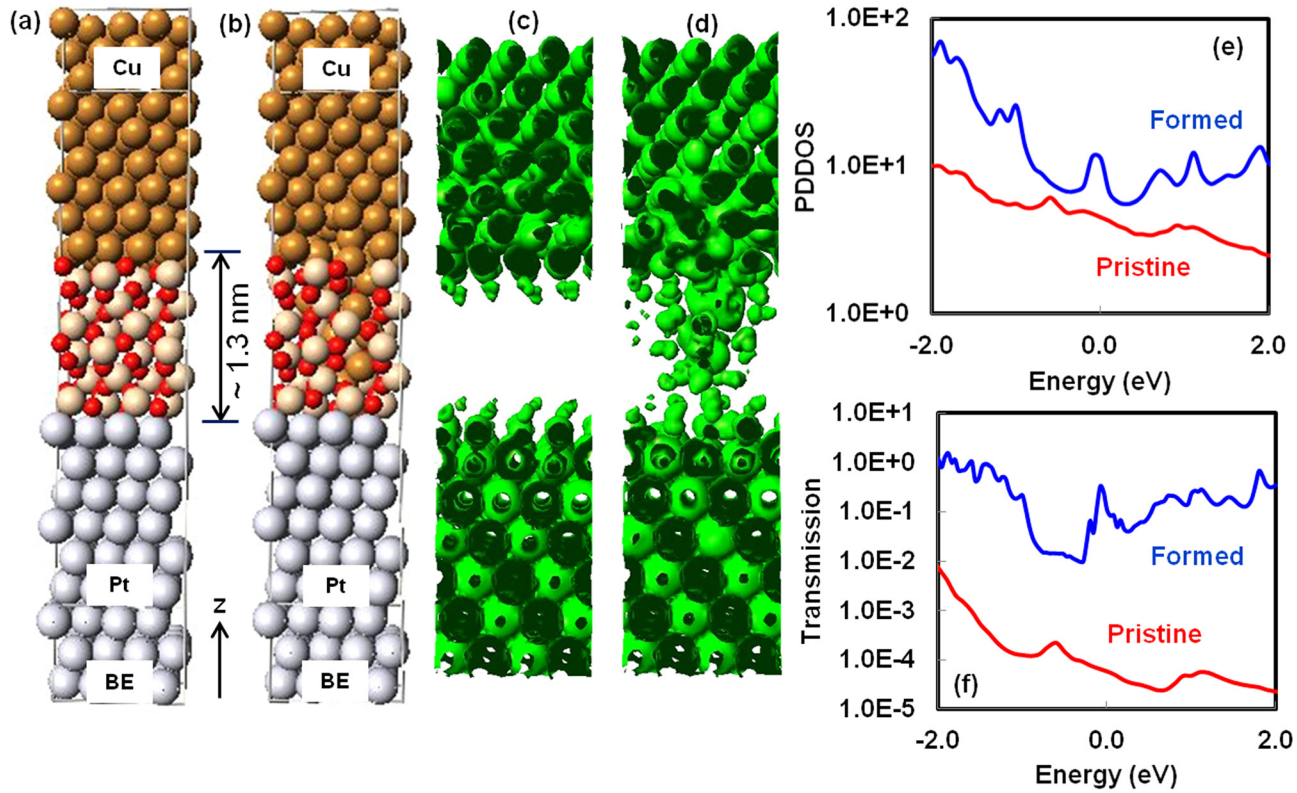

FIG. 8. Cu-SiO_2-Pt structures in (a) pristine and (b) formed states, and their corresponding local density of states at the Fermi-level (isosurface of electron concentration at 0.008 e/Å^3) (c) and (d). Comparison of (e) projected device density of states, and (f) transmission spectra in the pristine and formed states.

applied as deviation from ideal bond-angles and the mixing scaling factors are applied to Si-Cu and Cu-O bonds.

The thus far discussed thermodynamics of aggregation/isolation and impurity segregation at electrodes greatly influence the conductance and retention behavior; however, additional dynamical simulations are required to capture the forming of complex morphologies within a MIM system. The impurity concentration and distribution in the post forming-step are crucial in setting up the electrical characteristics of the cell. During the reset and set operation, these impurities ionize and migrate under fields to yield the metastable conductance states (which in addition influences the intrinsic noise and variability of these cells). To gain insights into the migration under fields, the cell dynamics up to 1 ns under a uniform field of ~10 MV/cm during forming has been simulated in this work. The molecular dynamics simulations were performed in a canonical (NVT) ensemble using a Noose-Hoover thermostat at T ~ 500 K. A system with periodic boundary conditions was assumed. The total simulation time of 1 ns was selected in order to capture experimental switching times, which are reported[4] to be in ~ns time scale at comparable electric fields. Moreover, 1 ns long runs allowed us to keep the simulations within reasonable compute times. The Cu clusters that are formed within the dielectric are expected to remain stable in the simulations at longer times, as shown in Figure 9, wherein structures are depicted for a MD run at four different simulation times. The structures at 0.75 ns and 1 ns appear to be relatively similar (as opposed to the ones at 0 ns and 0.25 ns that show substantial atomic rearrangements) indicating the system achieving stability at ~1 ns within our simulation conditions. In addition, we do not expect the thermal conditions in our simulations to be realistic after the insulator to metal transition is complete, due to the joule-heating that may arise from high electronic currents flowing through the structure. Hence, after a contact (a contiguous Cu path) is made, we do not continue the simulations. Fig. 10 shows the atomic structure for the pristine (a) and formed (b) cells, wherein Cu is the active electrode with an amorphous dielectric of ~1.2 nm SiO_2. Expectedly, the metal-ion shows an environment-dependent oxidation state with the Cu at the interface showing a higher oxidation state than at the bulk of the electrode, which is similar to the charge state of Cu being lower inside the cluster relative to the periphery of the agglomerate. Under an applied bias, the simulations show that the Cu ions at the interface oxidize and migrate in clusters and in the process attain variable charges through the dielectric (Fig. 9(b)). Due to the strong attractive correlation between the Cu ions, as well as a lower ionization when aggregated, Cu appears to prefer cluster migration at lower and moderate electric fields (≤10 MV/cm). The Cu ions near the active electrode largely migrate as clusters with thinner local Cu atomic-chains eventually forming near the bottom electrode interfaces. These $Cu^{\delta+}$ ions and the electric fields seem to significantly impact the structure of the insulator in the forming process as well. Cu near the interface (Fig. 5(c)) appears to be more oxidized than the Cu layers deeper into the electrode consistent with the as-prepared cell. The charges on the ions evolve in a coordination-dependent manner leading to the complex $Cu^{\delta+}$ charge distribution as shown in Fig. 9(b). The Cu ions

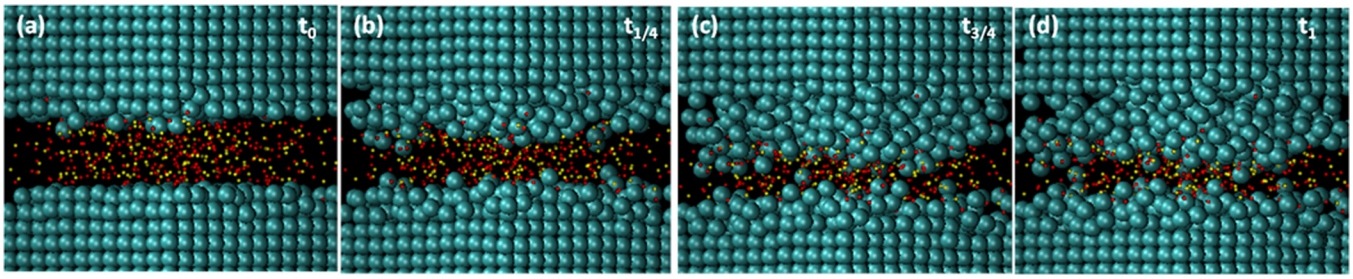

FIG. 9. Comparison of MD structures at various simulation times: (a) 0 ns, (b) 0.25 ns, (c) 0.75 ns, and (d) 1 ns. The large-cyan, small-yellow, and small-red spheres represent Cu, Si, and O, respectively.

are more positively charged on the periphery of the moving clusters than the ones inside with higher Cu-coordination. Although these simulations show unique physical insights into the forming mechanisms, due to the absence of a rigorous calculation of the local electric field and assumptions of no electron-phonon coupling (and the exclusion of the effects of non-adiabatic electron dynamics), the conductive bridge morphologies obtained may have limited bearing to physical reality. Since enhancement of local electric fields may lead to stronger anisotropy in migration that restricts the lateral confines of the evolving morphology along the field vector. This localization is also expected to compete and overcome the increased isotropic diffusion in the system arising from current-induced heating as the bridging (insulator-metal transition) is approached. Nevertheless, this work points to the need for further exploration of coupled electron-ion non-equilibrium dynamics accounting for electron and phonon transport towards a more accurate and predictive simulation framework.

III. SUMMARY AND CONCLUSIONS

We presented an atomic-scale description of physical processes of Cu metal impurity in insulators that are relevant to the operation of RRAM-M. Results from various simulation techniques are discussed that provide insight into the formation of lower- and higher-resistance states (LRS and HRS), retention, and device operation (forming/set/reset) of RRAM-M. The role of impurity concentration and distribution in determining the RS, the LRS-stability, electronic structure, and electron-conduction in such RS is numerically analyzed. Formation of Cu clusters in insulator led to greater than 3 orders of magnitude change in the electron transmission through a Cu-SiO_2-Pt MIM. In addition, the field induced barrier lowering calculations showed a small qualitative and quantitative difference in comparison to the literature. For the case of ion migration along the direction of the field, the lowering can be approximated in the form of a Mott-Gurney-like expression modified by a static dielectric constant.

The stability of RS (retention) was found to be governed by chemical dissociation in addition to the diffusion (dilute limit) of metal impurities. This was attributed to the chemical potential changes between the aggregated and isolated state of impurities. Furthermore, the thermodynamic preference of Cu for insulator-metal interfaces was shown across various combinations of insulator-metal interfaces, which is expected to strongly influence the Cu cluster morphology. Finally, the MD simulations under e-fields showed that the variably charged metal ions (from TE) in a MIM structure move in clusters along the field and stochastically form a conductive path in the insulator bridging the metallic electrode.

In conclusion, it is challenging to accurately model the operation of RRAM-M. Since it requires capturing of the chemical, thermal, and electronic processes that accompany ionic migration and long-range structural rearrangements. The analysis presented in this work, while interesting, is far from complete. In order to account for the conduction through localized paths in amorphous correlated oxides, a

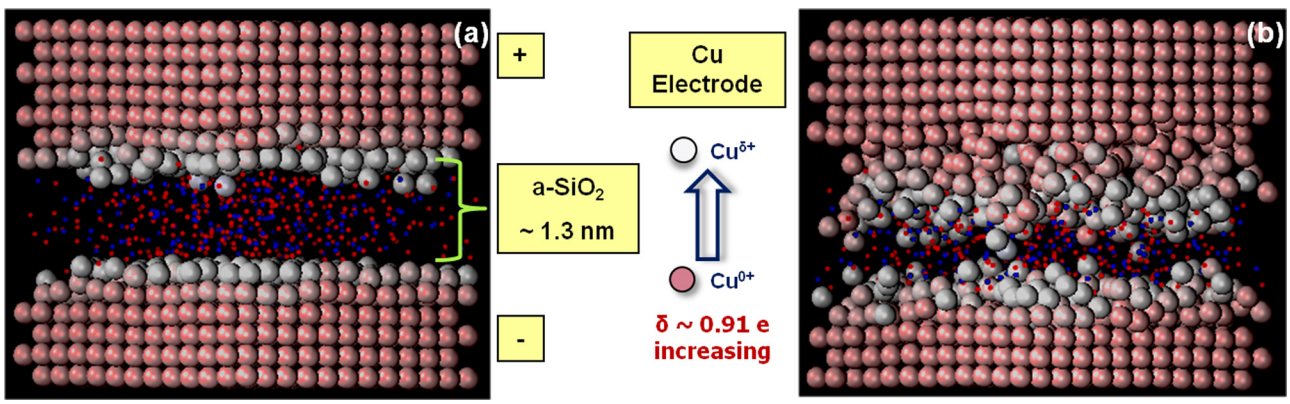

FIG. 10. Larger MIM cells (2.97 nm wide and 3.34 nm high consisting of 2377 atoms with an amorphous oxide) of Cu:a-SiO_2 generated through classical molecular dynamics simulations: (a) pristine and (b) formed. The charges on Cu ions are depicted as grey (darker) to white (lighter) with increasing oxidation state. The small blue and red atoms are Si and O atoms, respectively.

coupled electron-ion transport framework that includes electron-phonon coupling will have to be considered. This would enable a more accurate first-principles-based estimation of atomic arrangements during device operation and the corresponding electrical characteristics of RRAM-M.

ACKNOWLEDGMENTS

We gratefully acknowledge K. Prall, S. Sills, K. Holtzclaw, N. Ramaswamy, J. Smythe, and S. Kramer at Micron for their valuable discussions on technological challenges and relevance of the findings. In addition, the technical inputs on the computations from V. Eyert and A. Blom are sincerely acknowledged, along with the insightful discussions with A. H. Strachan from Purdue University.

[1]K. Aratani, K. Ohba, T. Mizuguchi, S. Yasuda, T. Shiimoto, T. Tsushima, T. Sone, K. Endo, A. Kouchiyama, S. Sasaki, A. Maesaka, N. Yamada, and H. Narisawa, in *IEEE International Electronic Devices Meeting* (2007), Vol. 7, p. 783.
[2]M. N. Kozicki, M. Balakrishnan, C. Gopalan, C. Ratnakumar, and M. Mitkova, in *IEEE Non-Volatile Memory Technology Symposium* (2005), Vol. 5, p. 83.
[3]B. M. Kope, M. Tendulkar, S.-G. Park, H. D. Lee, and Y. Nishi, Nanotechnology **22**, 254029 (2011).
[4]C. Schindler, G. Staikov, and R. Waser, Appl. Phys. Lett. **94**, 072109 (2009).
[5]J. R. Jameson, N. Gilbert, F. Koushan, J. Saenz, J. Wang, S. Hollmer, and M. N. Kozicki, Appl. Phys. Lett. **99**, 063506 (2011).
[6]I. Valov, R. Waser, J. R. Jameson, and M. N. Kozicki, Nanotechnology **22**, 254003 (2011).
[7]L. Goux, K. Sankaran, G. Kar, N. Jossart, K. Opsomer, R. Degraeve, G. Pourtois, G.-M. Rignanese, C. Detavernier, S. Clima, Y.-Y. Chen, A. Fantini, B. Govoreanu, D. J. Wouters, M. Jurczak, L. Altimime, and J. A. Kittl, in *VLSI Technology Symposium* (2012), p. 69.
[8]R. Meyer, L. Schloss, J. Brewer, R. Lambertson, W. Kinney, J. Sanchez, and D. Rinerson, in IEEE Proceedings, "Non-Volatile Memory Technology Symposium" (2008), Vol. 8, p. 1.
[9]D. B. Strukov and R. S. Williams, Appl. Phys. A **94**, 515 (2009).
[10]N. F. Mott and R. W. Gurney, *Electronic Processes in Ionic Crystals* (Dover Publications Inc., New York, 1964), p. 43.
[11]G. Kresse and J. Hafner, Phys. Rev. B **47**, 558 (1993); **49**, 14251 (1994); G. Kresse and J. Furthmuller, Comput. Mater. Sci. **6**, 15 (1996); **54**, 11169 (1996); MedeA, Materials Design, Inc., Angel Fire, NM, USA, 2015.
[12]J. P. Perdew, K. Burke, and M. Ernzerhof, Phys. Rev. Lett. **77**, 3865 (1996); **78**, 1396 (1997).
[13]P. E. Blochl, Phys. Rev. B **50**, 17953 (1994); G. Kresse and D. Joubert, *ibid*. **59**, 1758 (1999).
[14]J. Heyd, G. E. Scuseria, and M. Ernzerhof, J. Chem. Phys. **118**, 8207 (2003); **124**, 219906(E) (2006).
[15]R. D. King-Smith and D. Vanderbilt, Phys. Rev. B **47**, 1651 (1993).
[16]R. W. Nunes and X. Gonze, Phys. Rev. B **63**, 155107 (2001).
[17]I. Souza, J. Iniguez, and D. Vanderbilt, Phys. Rev. Lett. **89**, 117602 (2002).
[18]H. Eyring, J. Chem. Phys. **3**, 107 (1935).
[19]G. Henkelman, B. P. Uberuaga, and H. Jonsson, J. Chem. Phys. **113**, 9901 (2000).
[20]See www.quantumwise.com for Atomistix ToolKit version 12.8, QuantumWise A/S; M. Brandbyge, J.-L. Mozos, P. Ordejón, J. Taylor, and K. Stokbro, Phys. Rev. B **65**, 165401 (2002); J. M. Soler, E. Artacho, J. D. Gale, A. García, J. Junquera, P. Ordejón, and D. Sánchez-Portal, J. Phys.: Condens. Matter **14**, 2745 (2002).
[21]S. J. Plimpton, J. Comput. Phys. **117**, 1 (1995); S. J. Plimpton and A. P. Thomson, MRS Bull. **37**, 513 (2012).
[22]T.-R. Shan, B. D. Devine, S. R. Phillpot, and S. B. Sinnott, Phys. Rev. B **83**, 115327 (2011).
[23]T. V. Perevalov, A. V. Shaposhniko, V. A. Gritsenko, H. Wong, J. H. Han, and C. W. Kim, JETP Lett. **85**, 165 (2007).
[24]K. Xu, H. Sio, O. A. Kirillov, L. Dong, M. Xu, P. D. Ye, D. Gundlach, and N. V. Nguyen, J. Appl. Phys. **113**, 024504 (2013).
[25]N. F. Mott, Philos. Mag. **19**, 835 (1969); Adv. Phys. **16**, 49 (1967); P. W. Anderson, Phys. Rev. **109**, 1492 (1958); N. F. Mott, Philos. Mag. **26**, 1015 (1972); **32**, 961 (1975); N. F. Mott and E. Davis, *Electronic Processes in Non-Crystalline Materials* 1st ed. and 2nd ed. (Oxford University Press, 1971 and 1978).
[26]L. A. J. Garvie, P. Rez, J. R. Alvarez, P. R. Buseck, A. J. Craven, and R. Brydson, Am. Mineral. **85**, 732 (2000).
[27]S. Park, B. Lee, S. H. Jeon, and S. Han, Curr. Appl. Phys. **11**, S337 (2011).
[28]C.-Y. Liu, Y.-H. Huang, J.-Y. Ho, and C.-C. Huang, J. Phys. D: Appl. Phys. **44**, 205103 (2011).
[29]A. Belmonte, W. Kim, B. Chan, N. Heylen, A. Fantini, M. Houssa, M. Jurczak, and L. Goux, "90 nm WAl2O3TiWCu 1T1R CBRAM cell showing low-power, fast and disturb-free operation," *5th IEEE International Memory Workshop (IMW)*, 2013, pp. 26–29.